

Unravelling Solid-State Redox Chemistry in $\text{Li}_{1.3}\text{Nb}_{0.3}\text{Mn}_{0.4}\text{O}_2$ Single-Crystal Cathode Material

Wang Hay Kan,[†] Dongchang Chen,[†] Joseph K. Papp,[‡] Alpesh Khushalchand Shukla,[†] Ashfia Huq,[§] Craig M. Brown,^{||} Bryan D. McCloskey,^{†,‡} and Guoying Chen^{*,†}

[†]Energy Storage and Distributed Resources Division, Lawrence Berkeley National Laboratory, Berkeley, California 94720, United States

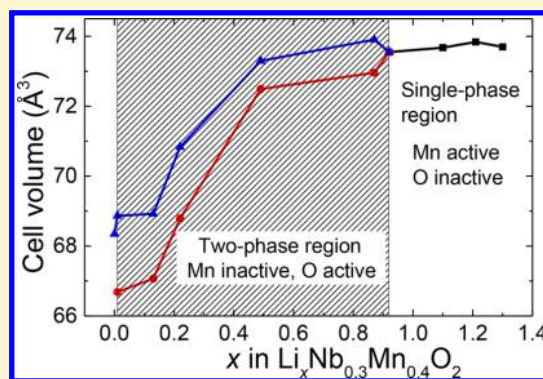
[‡]Department of Chemical and Biomolecular Engineering, University of California, Berkeley, California 94720, United States

[§]Neutron Scattering Science Division, Oak Ridge National Laboratory, Oak Ridge, Tennessee 37831, United States

^{||}Center for Neutron Research, National Institute of Standards and Technology 100 Bureau Drive Stop 6102, Building 235 Room A116, Gaithersburg, Maryland 20899-6102, United States

Supporting Information

ABSTRACT: Recent reports on high capacities delivered by Li-excess transition-metal oxide cathodes have triggered intense interest in utilizing reversible oxygen redox for high-energy battery applications. To control oxygen electrochemical activities, fundamental understanding of redox chemistry is essential yet has so far proven challenging. In the present study, micrometer-sized $\text{Li}_{1.3}\text{Nb}_{0.3}\text{Mn}_{0.4}\text{O}_2$ single crystals were synthesized for the first time and used as a platform to understand the charge compensation mechanism during Li extraction and insertion. We explicitly demonstrate that the oxidation of O^{2-} to O^{n-} ($0 < n < 2$) and O_2 loss from the lattice dominates at 4.5 and 4.7 V, respectively. While both processes occur in the first cycle, only the redox of $\text{O}^{2-}/\text{O}^{n-}$ participates in the following cycles. The lattice anion redox process triggers irreversible changes in Mn redox, which likely causes the voltage and capacity fade observed on this oxide. Two drastically different redox activity regions, a single-phase behavior involving only $\text{Mn}^{3+/4+}$ and a two-phase behavior involving $\text{O}^{2-}/\text{O}^{n-}$ ($0 \leq n < 2$), were found in $\text{Li}_x\text{Nb}_{0.3}\text{Mn}_{0.4}\text{O}_2$ ($0 < x < 1.3$). Morphological damage with particle cracking and fracturing was broadly observed when O redox is active, revealing additional challenges in utilizing O redox for high-energy cathode development.



1. INTRODUCTION

Lithium-ion batteries (LIBs) have become increasingly important for energy storage in portable electronics, electric vehicles, and stationary application in power grids. Since the discovery of early generations of cathode materials (e.g., LiCoO_2 and LiMn_2O_4) in the 1980s, only a few promising compounds with other compositions or crystal structures have been reported in the last three decades.^{1–3} The conventional wisdom suggests that in O3-type layered oxides, the 3d orbitals of early transition metals (TMs) are partially overlapped with the 2p orbitals of oxygen.⁴ As such, only about half of the 3d electrons are available to participate in the redox reaction, which largely limits practical capacity (for example, ~160 mAh/g for LiCoO_2) despite their much higher theoretical capacities. To develop high-energy batteries, cathodes with higher specific capacity (>200 mAh/g) and operating voltage (>4.3 V vs Li^+/Li) are needed.^{1–3}

Recently, approaches to enable high-energy cathodes by utilizing redox reactions of both TM cations and oxygen anions have triggered intense interest.^{5–7} One of the most studied examples is the lithium and manganese-rich (LMR) layered

oxides with a general formula of $\text{Li}_{1+x}\text{Mn}_{1-x-y-z}\text{Ni}_y\text{Co}_z\text{O}_2$.^{8–10}

Our recent work showed that, contrary to the common notion of a nanocomposite structure, the oxide has a single monoclinic phase ($C2/m$) with a large number of domains corresponding to different variants.¹¹ To involve the O 2p electrons in the following electrochemical reactions, the material typically undergoes an initial activation process signaled by a unique charging voltage profile that is much different from those of the subsequent cycles. Recent studies by Luo et al. suggested the formation of O^- holes in the intermediates, as evidenced by the progressive growth of a new peak on the O K-edge X-ray absorption spectroscopy (XAS) along with the use of a number of other characterization techniques, including isotopically labeled differential electrochemical mass spectroscopy (DEMS), X-ray absorption near edge structure (XANES), and resonant inelastic X-ray scattering (RIXS).⁹ However, this remains controversial as experimental evidence is difficult to

Received: December 1, 2017

Revised: February 9, 2018

Published: February 9, 2018

obtain, largely due to the high reactivity of O^- toward carbonate-based electrolyte to release carbon dioxide or self-combination of O^- to release oxygen. These processes also produce significant amount of oxide-ion vacancies in the unit cell, further destabilizing the crystal structure.¹² The activation process further triggers unfavorable phase transformations, possibly involving layered \rightarrow spinel \rightarrow rock-salt, as the cycling proceeds, leading to continuous voltage and capacity fades in the cathode.¹² Various optimization approaches such as doping,^{13,14} surface coating/engineering, and morphology control^{15–18} have been explored as means to mitigate the degradation, but all met with limited success.

An alternative approach to address the phase instability is to confine the O redox process within a rock-salt structure. This strategy was rarely used as it is generally believed that compounds with a rock-salt crystal structure lack lithium-ion conduction pathways and are therefore electrochemically inactive. In 2003, Shigemura et al. first reported that the Li/Ti/FeO₂ system can deliver a capacity of ca. 200 mAh/g at a slow rate of 10 mAh/g.^{19,20} Investigation on lithium-ion conduction pathways in rock-salt Li_{1.211}Mo_{0.467}Cr_{0.3}O₂ was then reported by Lee et al. in 2014.²¹ Using density functional theory (DFT) calculations, they revealed the percolation of active diffusion channels in disordered Li-excess materials. In 2015, Yabuuchi et al. reported a new rock-salt Li_{1.3}Nb_{0.3}Mn_{0.4}O₂ (LNMO) cathode with an impressive discharge capacity of ca. 300 mAh/g at 60 °C.²² With the use of soft/hard X-ray absorption spectroscopy, the authors proposed the involvement of both Mn^{3+/4+} and O²⁻/O⁻ redox reactions during charge. However, the detailed charge compensation mechanism and role of O, particularly the contribution from oxidation of O²⁻ to Oⁿ⁻ ($0 < n < 2$) and O loss from the lattice (in the form of O₂ gas, $n = 0$), remain unclear. In this study, well-formed Li_{1.3}Nb_{0.3}Mn_{0.4}O₂ single crystals were synthesized by a molten-salt method for advanced diagnostic studies. The use of single crystals allows us to perform additional single-particle-based studies for systematic comparison of the changes in crystal structure, chemical state, and microstructure as a function of lithium content in the sample. The results provide us important insights on O activities in the oxide sublattice and how to control/tune them through engineering strategies such as chemical composition and surface morphology control.

2. EXPERIMENTAL SECTION

2.1. Synthesis. In a typical crystal synthesis procedure, Li₂CO₃, Nb₂O₅, and Mn₂O₃ precursors (Sigma-Aldrich, >99%) were milled together with ethanol solvent at 200 rpm for 12 h in a planetary ball mill (RETSCH PM100) using a zirconia jar with zirconia balls. About 10–15 mol% of extra Li₂CO₃ was used to compensate Li loss that often occurs during high temperature heating. The dried powder was further mixed with KCl flux in a molar ratio of 2.5–5 between the flux and TM precursors (defined as R ratio hereafter). The obtained mixture was then heated at 950 °C for 12 h in an Ar atmosphere. A ramp rate of 4 °C/min was used for both heating and cooling. After the reaction, KCl was dissolved in deionized water, and the final product was obtained after filtration and thorough washing with water. Chemical delithiation of Li_{1.3}Nb_{0.3}Mn_{0.4}O₂ was achieved by reacting the pristine powder with various amounts of 0.1 M nitronium tetrafluoroborate (NO₂BF₄) in acetonitrile solution in an argon filled glovebox (O₂ < 1 ppm and H₂O < 1 ppm). The reaction was carried out at room temperature for 1–4 days. The resulting reaction mixtures were filtered, thoroughly washed with acetonitrile, and then dried overnight in a vacuum oven.

2.2. Characterization. Chemical composition of the samples was determined by an inductively coupled plasma optical emission spectrometer (ICP-OES 720 Series). Scanning electron microscopy (SEM) and energy dispersive X-ray spectroscopy (EDS) images were collected on a JEOL JSM-7500F field emission microscope at a 10 kV accelerating voltage. Prior to the analysis, the powder samples were sputtered with a thin top layer of Au to reduce the charging effect. Samples for transmission electron microscopy (TEM) experiments were prepared by drop casting a sonicated solution of the crystals in anhydrous ethanol onto a carbon coated TEM grid or by sectioning using focused ion beam. Selected area electron diffraction (SAED) was performed in TEM mode at 300 kV on the sectioned sample, while high angle annular dark field (HAADF) imaging was performed on dispersed particles in scanning transmission electron microscopy (STEM) mode at 120 kV, both using an FEI Titan electron microscope.

Phase purity was first analyzed by using laboratory X-ray diffraction (XRD) collected on Bruker D2 powder X-ray diffractometer (Cu K α , 40 kV, 30 mA). Synchrotron X-ray diffraction patterns were collected at ambient temperature at 11-BM at the Advanced Photon Source (APS) in Argonne National Laboratory, which operates with a monochromatic X-ray of $\lambda = 0.414$ Å. The scans were collected between 0.5° and 50° (2θ) at a step size of 0.0001°. The samples were first packed into Kapton capillary tubes before exposing to X-ray for 1 h. Time-of-flight (TOF) neutron diffraction data were collected at the POWGEN diffractometer at the Spallation Neutron Source, Oak Ridge National Laboratory. Samples were measured inside the vanadium sample cans, and a single bank wave with center wavelengths of 1.333 Å (2 h data collection) was used. Monochromatic (1.2 Å) neutron diffraction data were obtained using the high resolution powder diffractometer at BT1 at National Institute of Standards and Technology (NIST) Center for Neutron Research. The refinement of the diffraction data was carried out using GSAS/EXPGUI package.²³

Mn K-edge hard X-ray absorption spectra were collected in transmission mode using a (220) monochromator at SSRL beamline 2-2 and 2-3. The crystals were sandwiched between two Kapton films for data collection. Higher harmonics in the X-ray beam were reduced by detuning the Si (220) monochromator by 50% at the Mn edge. Energy calibration was accomplished by using the first inflection point at 6539 eV in the spectra of Mn metal foil reference. X-ray absorption near edge structure spectra were analyzed by Sam's Interface for XAS Package or SIXPACK software, with the photoelectron energy origin E_0 determined by the first inflection point of the absorption edge jump. Soft X-ray absorption spectroscopy measurements were carried out at beamlines 8-2 and 10-1 at SSRL. A thin layer of the oxide crystals was spread onto a conductive carbon tape which was then attached to an aluminum sample holder inside an Ar filled glovebox (O₂ < 1 ppm, H₂O < 1 ppm). Measurements were carried out on the 31-pole wiggler beamline 10-1 at SSRL with a ring current of 350 mA, a 1000 l mm⁻¹ spherical grating monochromator with 20 mm entrance and exit slits, a 0.2 eV energy resolution, and a 1 mm² beam spot. Data were collected at room temperature under ultrahigh vacuum (10⁻⁹ Torr) in a single load using the total electron yield and fluorescence yield mode detectors.

2.3. Electrochemistry. To prepare the composite electrodes, the active material was first ball-milled with acetylene carbon black (Denka, 20 wt %) to reduce the particle size and improve its electronic conductivity. The mixture was then mixed with acetylene carbon black and a polyvinylidene fluoride (PVdF) binder (Kynar 2801) in a 8:1:1 weight ratio in an NMP solvent. The slurry was spread onto aluminum foil and dried overnight at 120 °C under vacuum. Cathode disks with an area of 1.6 cm² and a typical electrode loading of 2–3 mg cm⁻² were cut from the electrode sheets and assembled into 2032-type coin cells in an argon-filled glovebox. Lithium foil (Alfa-Aesar) was used as counter and reference electrodes, Celgard 2400 polypropylene membrane as separators, and 1 M LiPF₆ in 1:1 (v/v) ethylene carbonate (EC):diethylene carbonate (DEC) (Novolyte Technologies Inc.) as electrolyte. The cells were galvanostatically cycled between 1.5 and 4.8 V using a VMP3 multichannel potentiostat/galvanostat controlled by EC-Lab v10.12 software (BioLogic Science Instru-

ments). Cyclic voltammetry tests were carried out using the same coin cell configuration with Li foil as counter and reference electrodes. The cells were scanned between 1.5 and 4.8 V with a constant scan rate of 5 mV/min. All electrochemical tests were carried out at room temperature.

Differential electrochemical mass spectroscopy measurements were performed in a customized Swagelok-type cell consisting of a lithium anode, a liquid electrolyte (1.0 M LiPF₆ in EC/DEC 1:1 v/v), and the crystal composite as the working positive electrode. The cell was periodically pulsed with Ar gas at regular intervals to sweep the evolved gases from the headspace to the mass spectrometer for analysis. The experimental setup is described in detail elsewhere.²⁴ Electrochemical measurements were carried out with a constant current rate of 25 mA/g between 1.5 and 4.8 V with a rest period of 25 min right after the cells reached the upper or lower cutoff voltages. All data were controlled by a BioLogic SP-300 potentiostat.

3. RESULTS AND DISCUSSION

3.1. Synthesis and Characterization of Li_{1.3}Nb_{0.3}Mn_{0.4}O₂ Single Crystals. Synthesis of polycrystalline Li_{1.3}Nb_{0.3}Mn_{0.4}O₂ cathode material was recently carried out by Yabuuchi et al.²² The process involved ball-milling stoichiometric amount of Li₂CO₃, Mn₂O₃, and Nb₂O₅, pressing the resulting mixture into a pellet, and then heating the pellet in Ar atmosphere at 900 °C for 24 h. Synthesis of Li_{1.3}Nb_{0.3}Mn_{0.4}O₂ single crystals, however, has not been reported in the literature. Here, we adopted a molten-salt method and systematically varied the synthesis conditions to obtain phase-pure and discrete Li_{1.3}Nb_{0.3}Mn_{0.4}O₂ single crystals with uniform morphology and size distribution for the first time. The following parameters were carefully optimized in our synthesis: choice of transition-metal precursor salts and flux salt, the molar ratio between the flux and TM precursors (R ratio), choice and amount of lithium precursor, heating temperature and time, and reaction atmosphere. It was found that the best reaction time and temperature were 12 h and 950 °C, respectively. Li₃NbO₄ was often obtained as an impurity when the reaction time was too short or the heating temperature was below 950 °C. The loss of lithium at elevated temperature was effectively compensated by using additional 10–15% of the lithium precursor. Various molten salts, including LiCl, NaCl, KCl, CsCl, KOH, and Li₂SO₄, were used as the flux, but only KCl (mp = 770 °C) led to the formation of phase-pure samples. The optimized R ratio was between 2.5 and 5. In addition, the presence of trace O₂ in the synthesis atmosphere can lead to the formation of Li₂MnO₃ and Li₃NbO₄ impurities.

The nominal composition of the as-synthesized oxide was analyzed by an inductively coupled plasma optical emission spectrometer, which confirmed the chemical formula of Li_{1.3}Nb_{0.3}Mn_{0.4}O₂. As shown in the scanning electron microscopy image in Figure 1a and high angle annular dark field scanning transmission electron microscopy (HAADF STEM) image in Figure 1b, the particles adopted a large spherical shape with an average size of ca. 5–8 μm and absence of any grain boundaries. This suggests that all the facets have similar thermodynamic stability and grow at a similar rate under current synthesis conditions. Contrast reversal toward the center of the particles observed in HAADF STEM images indicates that the pristine particles are too thick for detailed analytical electron microscopy. Focused ion beam (FIB) milling was then used to reduce the thickness and a SAED pattern in [110] zone axis was taken over an area covering almost entire single particle (Figure 1c). The pattern matches well with the

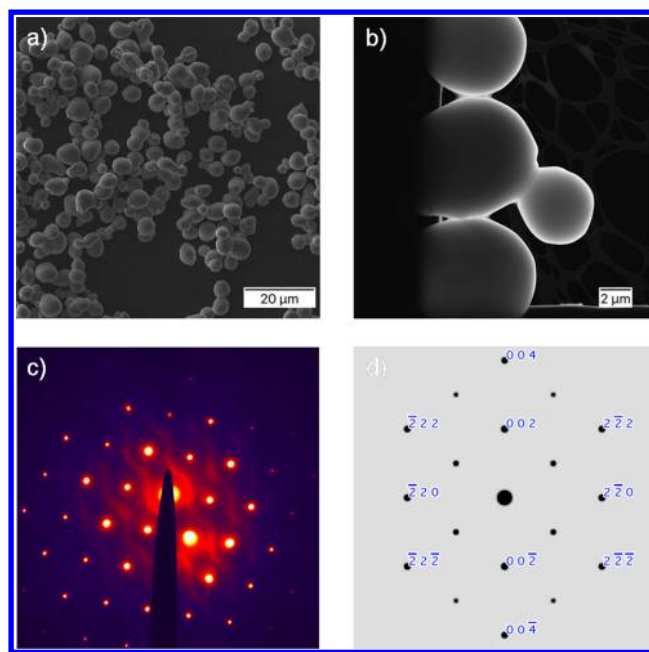


Figure 1. Morphology and structure of Li_{1.3}Nb_{0.3}Mn_{0.4}O₂ crystals: (a) secondary electron SEM image, (b) HAADF STEM image, (c) SAED pattern taken in [110] zone axis, and (d) simulated electron diffraction pattern corresponding to panel c.

one simulated using $Fm\bar{3}m$ structure with a lattice parameter of $a = 4.2 \text{ \AA}$ (Figure 1d), confirming the single crystal nature of the particle. It is worth noting that the SAED pattern from this particle also shows diffuse scattering effects that are characteristic of materials with short-range ordering.²⁵ At this point, it is unclear whether this short-range order occurs broadly in the entire sample or if it has any effect on oxide properties and behavior. Both of the questions require further investigation with complementary analytical techniques, and the results will be reported in a future publication.

Bulk phase purity and crystal structure of the synthesized samples were evaluated by using both synchrotron X-ray and neutron diffraction studies. Figure 2 shows the Rietveld refinement of the diffraction patterns, while Table 1 lists the refined structural parameter. In both sets of diffraction patterns, the high peak symmetry observed in a wide angular range indicates a single phase with high crystallinity. Rietveld refinement confirms a rock-salt crystal structure with a lattice parameter of 4.1954(1) Å and cell volume of 73.685(1) Å³, which is in good agreement with the values reported by Yabuuchi et al. on polycrystalline samples.²² All cations (Li, Nb, and Mn) were located in the 4a sites, and all M–O bonds had the same distance of 2.0965(1) Å, confirming the disordered nature of the oxide crystals. The refined occupancies agree well with the chemical formula of Li_{1.3}Nb_{0.3}Mn_{0.4}O₂. Note that short-range ordering was not fully investigated in this study but will be the topic of a follow up publication.

3.2. Electrochemical Studies. The electrochemical performance of Li_{1.3}Nb_{0.3}Mn_{0.4}O₂ crystals was evaluated at room temperature in a half-cell configuration. Due to high resistance and poor utilization of large particles, only limited capacities were obtained on composite electrodes made with the as-synthesized micrometer-sized crystals. In a modified procedure, the crystal size was reduced and electronic conductivity improved by ball-milling the oxide crystals together with a carbon black additive in a

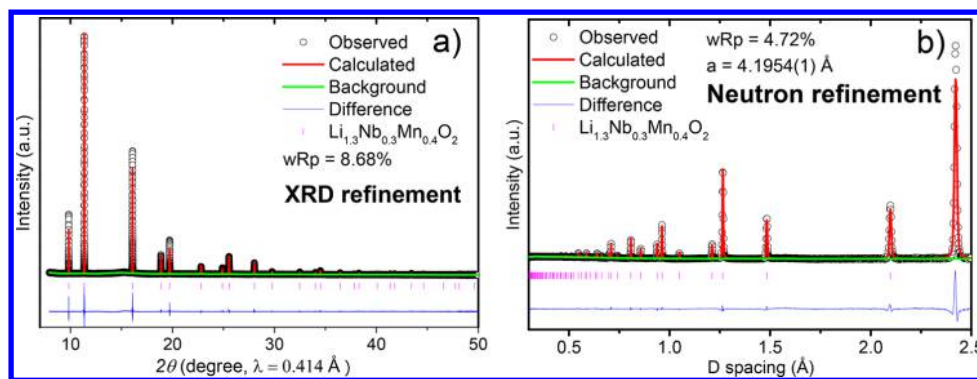


Figure 2. Rietveld refinement of (a) XRD and (b) neutron diffraction patterns collected on pristine $\text{Li}_{1.3}\text{Nb}_{0.3}\text{Mn}_{0.4}\text{O}_2$ single crystals (POWGEN). Values in parentheses indicate standard deviation.

Table 1. Structural Parameters of Pristine $\text{Li}_{1.3}\text{Nb}_{0.3}\text{Mn}_{0.4}\text{O}_2$ Crystals Determined from Joint Rietveld Refinements of Synchrotron X-ray and TOF Neutron Data^a

atom	position	Wyck. site	occip.	$d_{(M-O)}$ (Å)	bond valence	$100(U_{\text{iso}})$ (Å ²)
Li	0,0,0	4a	0.65	2.0965(1)	1.092	1.13(1)
Mn	0,0,0	4a	0.2	2.0965(1)	2.43	1.13(1)
Nb	0,0,0	4a	0.15	2.0965(1)	3.66	1.13(1)
O	0,0,0.5	4b	1.0	2.9650(1)		1.72(1)

^a $Fm\bar{3}m$, a (Å) = 4.1954(1) V (Å³) = 73.845(1), wR_p = 9.22%, δ = 0.0(0).

$\text{Li}_{1.3}\text{Nb}_{0.3}\text{Mn}_{0.4}\text{O}_2$:carbon weight ratio of 80:20. A SEM image of the mixture is shown in Figure S1. The mixture was then added into the standard carbon and PVdF slurry in an N-

methyl-2-pyrrolidone (NMP) solvent and cast onto the Al current collector. The final weight ratio of active material:carbon additive:PVdF binder in the thus-prepared electrodes was 56:34:10. Electrode disks with a size of 1.6 cm² and an active material loading of ca. 2–3 mg/cm² were then cut out and used as cathodes in coin cells, which were cycled between 1.5 and 4.8 V vs Li⁺/Li at a constant current density of 10 mA/g. Figure 3a shows the voltage profiles of the first four cycles. Similar to what was observed in the LMR oxide cathodes, two distinct regions, a sloping region and a plateau region, are present during the first charge. In the sloping region, the voltage increased steadily from the open circuit voltage (OCV) of 3.0 to 4.3 V, which delivered a specific capacity of ~115 mAh/g. Whereas in the plateau region, the voltage increased only slightly from 4.3 to 4.5 V before it rapidly increased to the

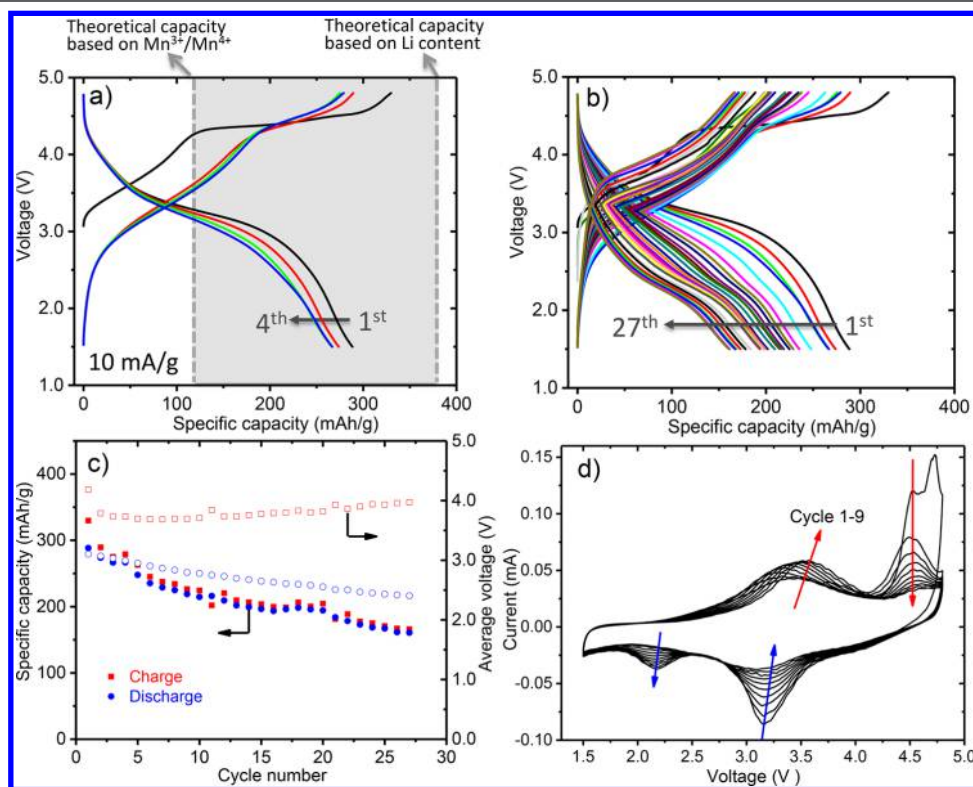


Figure 3. (a and b) Voltage profiles of $\text{Li}_{1.3}\text{Nb}_{0.3}\text{Mn}_{0.4}\text{O}_2$ half-cell cycling. (c) Specific capacity and average voltage as a function of cycle number. (d) Cyclic voltammogram of the first 9 scans at a scan rate of 5 mV/min. Solid symbols and open symbols in panel c represent capacity and voltage, respectively.

cut off voltage of 4.8 V. A specific capacity of ~ 215 mAh/g was obtained above 4.3 V on the first cycle, leading to a total charge capacity of 330 mAh/g. An overall sloping discharge profile was observed, which delivered a total discharge capacity of ~ 290 mAh/g at the cutoff voltage of 1.5 V. The Coulombic efficiency for the first cycle is therefore $\sim 88\%$. Two guidelines, one showing the theoretical capacity originated from the $\text{Mn}^{3+}/\text{Mn}^{4+}$ redox couple at 118 mAh/g and the other showing the theoretical capacity based on Li content at 383 mAh/g are also shown in Figure 3a. It is clear that both charge and discharge capacities (330 and 290 mAh/g, respectively) are significantly larger than the theoretical capacity of the $\text{Mn}^{3+}/\text{Mn}^{4+}$ redox (118 mAh/g). The charge capacity obtained in the sloping region is consistent with the capacity from the $\text{Mn}^{3+}/\text{Mn}^{4+}$ redox couple, suggesting that $\text{Mn}^{3+}/\text{Mn}^{4+}$ may be the sole redox process occurring in this region below 4.3 V.

In the second cycle, there is an overall decrease in the charging voltage of the sloping region, which led to an increased capacity of ~ 180 mAh/g upon reaching 4.3 V. The plateau region became somewhat sloping, but voltage increase remained slow. With cycling, the degree of sloping gradually increased, and the capacity obtained from this plateau region continued to decrease. The same trend was also observed on the discharge capacity, which was reduced to 160 mAh/g after 27 cycles, a loss of nearly 45% (Figures 3b and c). These results obtained from room-temperature cycling are comparable to what was obtained at 60 °C by Yabuuchi et al. Although more carbon was used in our electrode, which likely contributed to the improved performance, the results may also indicate that the crystal samples have a kinetic advantage compared to the polycrystalline samples synthesized using the solid-state method. Further analysis showed that the oxide experienced not only capacity fade but also voltage fade. As shown in Figure 3c, the average discharge voltage, obtained by dividing the total cell energy (E) by the cell capacity (Q) at 1.5 V, continues to decrease along with cycling. The extent of decay appears to be sensitive to the discharge cutoff voltage, and much faster decay was observed when the cutoff voltage was reduced from 1.5 to 1.0 V.

Further insights on the redox activities of $\text{Li}_{1.3}\text{Nb}_{0.3}\text{Mn}_{0.4}\text{O}_2$ crystals were obtained from cyclic voltammetry performed between 1.5 and 4.8 V at a scan rate of 5 mV/min. Figure 3d shows the results obtained from the first nine cycles. A broad peak centered at 3.5 V and a split peak between 4.5 and 4.7 V were observed during the first oxidation, corresponding to the sloping and plateau regions on the charging voltage profile, respectively. In the following scans, the oxidation peak at 3.5 V gradually moves toward high voltage, and its intensity grew while that of the peak at 4.5 V decreased, along with the disappearance of the split peak at 4.7 V after the first cycle. As the peak around 4.5–4.7 V is often attributed to the oxidation of O^{2-} to O^{n-} ($0 \leq n < 2$), the disappearance of the split peak and the continuous decrease in peak intensity suggest the complex and irreversible nature of the processes. During the first reduction, only a single peak was observed around 3.2 V, which decreased its intensity along with the appearance and gradual growth of a new peak around 2.2 V in the following scans. The pair of peaks centered at 3.5 V during oxidation and 3.2 V during reduction is likely associated with the $\text{Mn}^{3+}/\text{Mn}^{4+}$ redox couple. The growth of the reduction peak at 2.2 V at the expense of the peak at 3.2 V suggests the gradual transformation of the Mn species and the increasing contribution from the lower voltage process along with cycling. This

transformation was not observed when the upper cutoff voltage was limited to 4.0 V, before the onset of the oxygen oxidation peak. The results suggest that the oxidation of O^{2-} to O^{n-} at high voltage may be responsible for the irreversible conversion of the Mn^{3+} redox species, which ultimately led to both capacity and voltage fade in this oxide cathode.

Operando differential electrochemical mass spectroscopy was used to further examine the oxidation process of O^{2-} to O^{n-} ($0 \leq n < 2$) occurring between 4.5 and 4.7 V. Figure 4 shows the

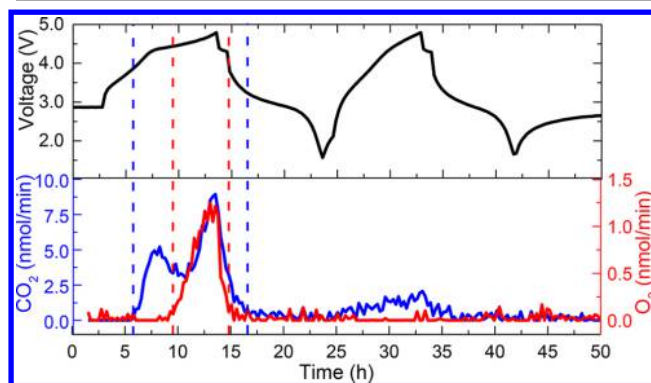


Figure 4. (a) Voltage profile and (b) O_2 and CO_2 gas evolution analyzed by DEMS of a cathode containing 2.66 mg $\text{Li}_{1.3}\text{Nb}_{0.3}\text{Mn}_{0.4}\text{O}_2$ active material.

results obtained during the first 2 cycles at a constant current density of 25 mA/g. The voltage profiles are similar to those obtained from the coin cell tests, validating the excellent quality of the in situ electrochemical cell. During the first cycle, both CO_2 and O_2 evolution were detected. CO_2 evolution began around 3.8 V during the charge (the first blue guideline in the figure) and completed around the mid-discharge cycle (the second blue guideline). There was an increase in intensity around the midplateau after the onset of O_2 evolution, and the peak CO_2 evolution was reached at the end of charge at 4.8 V. Oxygen gas was not detected until the midplateau region at about 4.5 V (the first red guideline in the figure), which also peaked at the upper cutoff voltage of 4.8 V. Oxygen evolution completes at the beginning of first discharge after the resting step (the second red guideline). The cumulative CO_2 and O_2 evolved from the first cycle were 1.53 and 0.11 μmol , respectively, from a cathode that contained 2.66 mg of active materials. Oxygen evolution, therefore, is much reduced compared to what was reported on the lithium and manganese-rich layered oxide system by Luo et al.^{9,10} In the second cycle, the amount of CO_2 was reduced from 1.53 to 0.46 μmol , while negligible O_2 evolution was detected.

Several sources may contribute to the evolution of CO_2 gas. Li_2CO_3 , a precursor from synthesis or a byproduct formed during air exposure of Li-TM oxide samples, can decompose during charging and release CO_2 gas. Recent studies confirmed that in LMR oxide cathodes,²⁶ all CO_2 gas evolved during the first charge in the typical voltage region results from residual Li_2CO_3 in the samples. Given the similar outgassing behavior of $\text{Li}_{1.3}\text{Nb}_{0.3}\text{Mn}_{0.4}\text{O}_2$ cathode to LMR, we postulate that residual Li_2CO_3 likely accounts for most, if not all, CO_2 evolution observed in Figure 4. Nevertheless, carbonate-based electrolytes are usually unstable at voltages above 4.3 V, especially in the presence of high valence transition metals (such as Mn^{4+}) that may catalyze the process and further lower the decomposition voltage, and a small percentage of CO_2 evolution at high

potentials may originate from this degradation process. Carbonate solvent decomposition due to the attack of oxygen species has also been reported in the context of Li–O₂ batteries.^{27–29} This represents another possible mechanism for lattice oxygen loss in addition to oxygen gas evolution. In the simplest case where we safely assume only O atoms in O₂ gas originate from Li_{1.3}Nb_{0.3}Mn_{0.4}O₂ cathode material, the total lattice O loss from a cathode containing 2.66 mg of active materials was 0.11 μmol, which corresponds to 0.38 mol % of oxygen ion vacancy in the delithiated cathode and a capacity of 4.48 mAh/g. Although some of the first charge capacity may also come from Li₂CO₃ oxidation to CO₂ via a 2 e[−]/CO₂ process and side reactions from electrolyte decomposition, it is evident that the redox process of O^{2−} to O^{*n*−} (0 < *n* < 2) species accounts for the majority of the first charge capacity above 4.3 V (215 mAh/g) and the first discharge capacity (290 mAh/g) in Li_{1.3}Nb_{0.3}Mn_{0.4}O₂ cathode.

The DEMS results also reveal that capacity contribution from O extraction from the oxide lattice occurs above ~4.5 V. This mechanism is active during the first charge which disappears in the following cycles. This is consistent with the observation on the CV studies, where the oxidation peak centered at 4.7 V was observed only during the first scan. The combined results suggest that the peak at 4.7 V is likely related to O^{2−} oxidation to O₂ gas. The peak centering at 4.5 V, therefore, is attributed to the oxidation O^{2−} anion to O^{*n*−} (0 < *n* < 2) species. While both O₂ gas evolution and lattice oxygen oxidation occur in the first charge, the following cycles involve only the redox of O^{2−} to O^{*n*−} (0 < *n* < 2) species, signaled by the single oxidation peak at 4.5 V. The continuous decrease in peak intensity along with scanning indicates that the lattice anion redox process is highly irreversible. After merely nine cycles, the O redox process no longer participates.

3.3. Structural, Chemical, and Morphological Evolution during the First Delithiation. To gain further insights on structural and chemical changes during the first charge, we resorted to chemical delithiation, which allows for the preparation of samples in the large quantity needed for a number of analytical techniques. This approach also allows us to monitor morphological evolution as large single crystals can be used directly without the prior milling process, a necessary step to electrochemically charge and discharge the sample. Pristine Li_{1.3}Nb_{0.3}Mn_{0.4}O₂ crystals were mixed with various amount of nitronium tetrafluoroborate oxidant in acetonitrile to prepare a series of Li_{*x*}Nb_{0.3}Mn_{0.4}O₂ (*x* = 1.21, 1.1, 1.06, 1.03, 0.92, 0.87, 0.81, 0.76, 0.64, 0.56, 0.49, 0.40, 0.32, 0.22, 0.13, 0.01, and 0) samples at different states of charge, which were subsequently examined by synchrotron X-ray and neutron diffraction, hard and soft X-ray absorption spectroscopy, and SEM. While the Li content was determined by ICP measurements, the Mn/Nb ratio in each sample was verified to be consistent with the calculated value of 1.33 by using energy dispersive X-ray spectroscopy. Figure 5a shows the powder XRD patterns collected at 11-BM at the Advanced Photon Source. As discussed earlier, the pristine Li_{1.3}Nb_{0.3}Mn_{0.4}O₂ is phase pure with a rock-salt crystal structure (*Fm* $\bar{3}$ *m*; *a* = 4.1954(1) Å). The 4a sites are occupied by Li, Nb, and Mn cations, whereas the 4b sites are occupied only by O anions. Oxygen vacancy was not detected in the pristine sample. With Li extraction, a single rock-salt phase remained when the lithium content is above 0.9 (*x* > 0.9). Further removing Li from the structure led to peak broadening and peak shifting toward to high angle, suggesting an overall

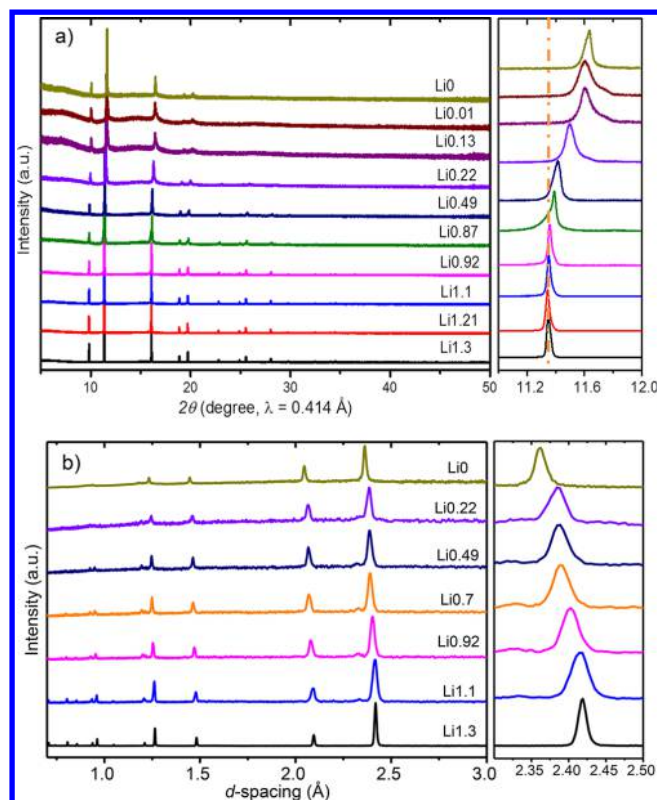


Figure 5. (a) Synchrotron X-ray diffraction and (b) monochromatic neutron diffraction patterns collected on chemically delithiated Li_{*x*}Nb_{0.3}Mn_{0.4}O₂ crystals. For neutron measurement, Li1.3 and Li0 samples were measured at SNS (POWGEN) using TOF, while Li1.1, Li0.92, Li0.7, Li0.49, and Li0.22 samples were measured at NIST (BT-1) using a single wavelength of $\lambda = 1.19$ Å. Note that the Li contents were determined by ICP measurements where an error range of up to ± 0.06 is possible.

reduction in lattice dimension. Similar results were also observed in neutron patterns collected on several samples in the series, as shown in Figure 5b. Joint X-ray and neutron Rietveld refinement was performed in cases where the same sample was examined by both techniques. Figure S2 and Table 2 show the results obtained from Rietveld refinement of these XRD patterns. The structural transformation can be separated into two regions: single phase (phase 1) behavior when *x* > 0.9 (region I) and a two-phase (phase 2 and 3) behavior when 0 < *x* < 0.9 (region II). The unit cell volume and phase fraction as a function of Li content were constructed from the refinement and shown in Figures 6a and b, respectively. The Vegard's law is only followed in region I, where the total volume change is ca. 0.2%. This is consistent with the participation of simple cation redox from Mn³⁺ to Mn⁴⁺ along with the extraction of 0.4 Li⁺ from the Li_{1.3}Nb_{0.3}Mn_{0.4}O₂ structure. Complex mixed oxygen activities are likely involved in region II, where phases 2 and 3 with the same rock-salt crystal structure but different lattice dimension evolve along with the extraction of Li. Smaller sized phase 3 reaches the maximum fraction when *x* is ~0.5, whereas phase 2 becomes the main phase with further Li removal. Combining with the results from the electrochemical studies, we propose that lattice O^{2−} oxidation to O^{*n*−} (0 < *n* < 2) mainly occurs in phase 3, whereas loss of O from the lattice mainly occurs in phase 2. This was further supported by results from the joint X-ray and neutron refinements (Figure S3), which revealed that ~2 and 7.8 mol % of oxygen ion vacancies

Table 2. Summary of Structural Parameters in $\text{Li}_x\text{Nb}_{0.3}\text{Mn}_{0.4}\text{O}_{2-\delta}$ ($0 \leq x \leq 1.3$) Determined from Rietveld Refinement of Synchrotron X-ray Diffraction and Neutron Data^a

x	1.3	1.21	1.1	0.92	0.87	0.49	0.22	0.13	0.01	0
V_1 (Å ³)	73.845(1)	73.839(1)	73.689(1)	73.544(1)						
V_2 (Å ³)					73.84(1)	73.295(1)	70.838(1)	68.93(1)	68.89(1)	
V_3 (Å ³)					72.877(2)	72.494(1)	68.80(2)	67.07(3)	66.69(1)	68.34(1)
n_1	1.0	1.0	1.0	1.0						
n_2					0.57(1)	0.24(1)	0.93(1)	0.84(1)	0.93(1)	
n_3					0.43(1)	0.76(1)	0.07(1)	0.16(1)	0.07(1)	1.0
d_1 (Å)	2.0965(1)	2.0976(1)	2.0962(1)	2.0948(1)						
d_2 (Å)					2.0976(5)	2.0736(7)	2.0690(2)	2.0500(4)	2.0495(3)	
d_3 (Å)					2.0885(4)	2.0667(4)	2.0541(3)	2.0315(3)	2.0276(7)	2.0444(1)
$100(U_{\text{iso}1})$ (Å ²)	1.13(1)	1.22(1)	1.44(1)	1.47(1)						
	1.72(1)	1.90(1)	2.18(1)	2.28(2)						
$100(U_{\text{iso}2})$ (Å ²)					1.55(3)	2.39(1)	4.11(1)	4.75(6)	3.03(4)	
					2.53(5)	3.15(1)	4.85(1)	6.08(9)	3.59(5)	
$100(U_{\text{iso}3})$ (Å ²)					2.92(4)	2.39(1)	4.11(1)	4.75(6)	3.03(4)	5.46(6)
					2.75(6)	3.15(1)	4.85(1)	6.08(9)	3.59(5)	6.15(8)
δ	0(0)		0(0)			0(0)	0.02(1)			0.08(1)
wR_p (%)	9.22	6.78	6.85	7.40	7.25	8.91	6.71	8.70	6.91	8.16

^a V_1 , V_2 , V_3 , n_1 , n_2 , n_3 , d_1 , d_2 , d_3 , $U_{\text{iso}1}$, $U_{\text{iso}2}$, and $U_{\text{iso}3}$ represent the unit cell volume, phase fraction, bond distance of Li/Mn/Nb–O), and thermal factors for Li/Nb/Mn and O in phase 1, 2, and 3, respectively. δ represents oxygen anion vacancy in each phase, while wR_p represent the residual factor of the refinement.

exist in the delithiated $\text{Li}_x\text{Nb}_{0.3}\text{Mn}_{0.4}\text{O}_{2-\delta}$ with $x = 0.2$ and 0 , respectively. Compared to the oxygen ion vacancies in the electrochemically charged samples, the much higher concentration is likely due to the fact that chemical delithiation was performed in an open system that shifts the equilibrium toward more gas evolution. We also like to point out that protons were detected on the chemically delithiated oxides based on the prompt-gamma activation analysis (PGAA). This is likely molecular in nature as delithiated samples generally have higher surface area (as shown in the SEM images in Figure 9) and tend to absorb water during brief air exposure. However, it is possible that the detected protons may originate from cation exchange between Li^+ and H^+ , as previously reported on the classic layered oxides.³⁰ Further analysis is needed to fully understand the source of protons in these samples.

The kinetic properties of delithiation were evaluated by the relationship between the molar ratio of oxidant/oxide used and the residual Li content in the sample (Figure 6c), as determined by ICP. While a linear relationship is apparent in region I, significant deviation is seen in region II, further confirming the complex nature of mixed anion activities at lower Li contents.

Hard X-ray absorption spectroscopy correlates the changes in the absorption edge energy to the variations in the average oxidation state of the absorbing atoms being analyzed in the bulk material.^{31,32} The technique also probes the local and electronic structures near the absorbing atoms and has the ability to reveal element-specific structural changes in the samples. Due to the energy limit of the XAS beamline at SSRL, Nb spectra were not collected in this study. A previous report from Yabuuchi et al. indicated that Nb remains at 5+ during the entire charge/discharge process.²² The normalized spectra of Mn *K*-edge and XANES spectra of the chemically delithiated $\text{Li}_x\text{Nb}_{0.3}\text{Mn}_{0.4}\text{O}_2$ series are shown in Figures 7a and b, respectively. The spectrum of pristine $\text{Li}_{1.3}\text{Nb}_{0.3}\text{Mn}_{0.4}\text{O}_2$ is consistent with that of Mn^{3+} collected on the standard reference. Substantial blue-shift of the edge energy was observed as the lithium content was reduced from 1.3 to 0.9, consistent with the oxidation of Mn^{3+} to Mn^{4+} . Negligible

changes were observed in samples with the Li content below 0.9. The edge position, defined by Photoelectron Energy Origin (E_0), is a commonly used parameter for extracting edge energy level in XANES spectra.³³ Figure 7c compares the edge position as a function of lithium content in $\text{Li}_x\text{Nb}_{0.3}\text{Mn}_{0.4}\text{O}_2$ samples. It is clear that Mn *K*-edge energy shifts toward higher value in a near linear fashion when $x > 0.9$ (region I) whereas it remains nearly constant when $0 < x < 0.9$ (region II). This is consistent with the results from X-ray and neutron diffraction studies, further confirming that Mn is only redox active in region I.

Further changes were observed in the intensity of Mn pre-edge absorption peaks arising from the dipole forbidden $1s \rightarrow 3d$ electronic transitions, which are typically weak in the transition metals. In the presence of 3d and 4p orbital hybridization, often resulting from structural distortion in local symmetry or noncentrosymmetric environment between the metal and oxygen coordination, the transitions are made partially allowed, and the peaks become much stronger.^{34–36} As shown in Figure 7d, the intensity of the pre-edge absorption peaks is similar in region I, which becomes noticeably stronger in region II. This suggests that although Mn redox activities are not involved in region II, the nature of Mn–O bond is altered in these samples, providing further evidence for oxygen redox activities in this region as the processes are likely behind the changes in local symmetry and environment of metal–ligand coordination. Similar to the edge shift observed in Figures 7a and b, the absorption energy of the pre-edge peaks also experienced blue shift in region I while maintaining nearly constant in region II, corroborating with the observation of Mn redox activity in region I only.

Oxygen redox activities during delithiation of $\text{Li}_{1.3}\text{Nb}_{0.3}\text{Mn}_{0.4}\text{O}_2$ were investigated by soft XAS that directly probes the chemical changes of the element as a function of penetration depth. The depth profiling from the surface to bulk were achieved by using two different detectors in total electron yield (TEY) and fluorescence yield (FY) modes, which have a typical probing depth of 5 and 50 nm, respectively.³⁷ Figures 8a and b show the evolution of TEY and FY O *K*-edge XAS

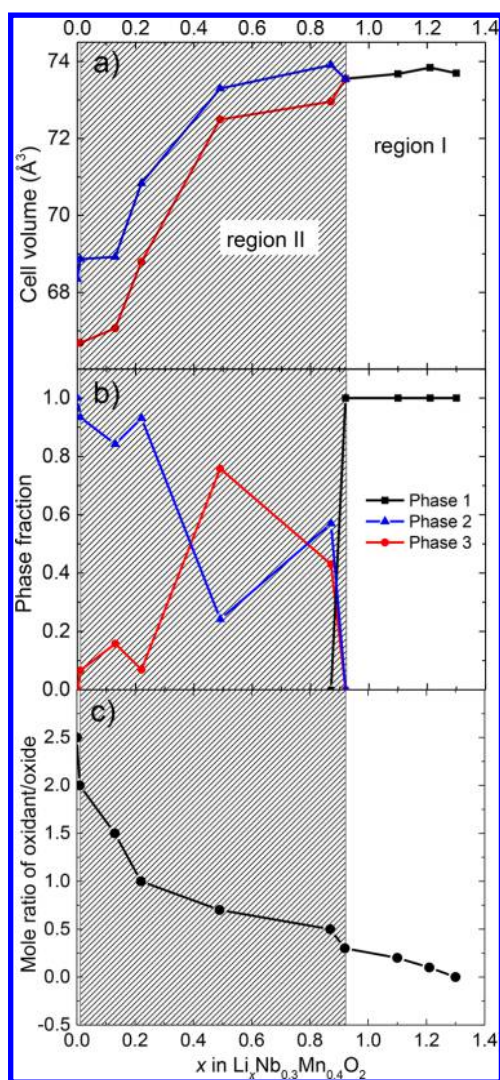


Figure 6. (a and b) Cell volume and phase fraction as a function of x in delithiated $\text{Li}_x\text{Nb}_{0.3}\text{Mn}_{0.4}\text{O}_2$ samples and (c) relationship between the molar ratio of oxidant/oxide and residue Li content in chemically delithiated $\text{Li}_x\text{Nb}_{0.3}\text{Mn}_{0.4}\text{O}_2$ samples.

spectra as a function of Li content in $\text{Li}_x\text{Nb}_{0.3}\text{Mn}_{0.4}\text{O}_2$. In both cases, the spectra can be separated into the pre-edge region and postedge region at the black dashed line (533 eV) shown in the figures. Features in the postedge region are often attributed to $\text{O}1s \rightarrow \text{O}2p\text{-TM}4s4p$ hybridization, while those in the pre-edge region are attributed to $\text{O}1s \rightarrow \text{O}2p\text{-TM}3d$ hybridization.^{38,39} Due to the crystal field effect and octahedral coordination of oxygen, the pre-edge peaks are often represented by multiplets between 528 and 533 eV. As the $\text{O}2p$ and $\text{TM}3d$ band electrons are of most interest to redox activities, we focus on the analysis in the pre-edge region. It is clear that as lithium is extracted from $\text{Li}_{1.3}\text{Nb}_{0.3}\text{Mn}_{0.4}\text{O}_2$, both TEY and FY spectra exhibit a significant increase in the pre-edge peak intensity. This increase is often used as a qualitative measure for the generated holes left by electron extraction from either oxygen or TM at the $\text{O}2p\text{-TM}3d$ energy levels.^{39–41} A new shoulder peak at ~ 529 eV also appeared and gradually grew along with delithiation, suggesting the involvement additional O-TM hybridization (referred to as p -band) during the process. Due to similarity between the p -band and the pre-edge absorption peak often observed in peroxides and superperoxides,^{22,40,42,43}

we speculate this new O-TM hybridization arises from the interaction between oxygen anions as a result of oxygen redox activities. Note that similar results were previously reported on the LMR cathode materials.^{22,40}

To better understand the oxygen redox activities as a function of Li content, quantifications of peak features in both TEY and FY O K -edge XAS spectra were performed, and the results are shown in Figures 8c and d. The detailed peak fitting method is also shown in Figure S4. For both TEY and FY spectra, the ratio between the pre-edge peaks and postedge peaks continuously increase with lithium extraction, as shown in Figure 8c. This confirms electron extraction from $\text{O}2p$ and TM $3d$ hybridization and agrees with the previous report by Yabuuchi et al.²² It is, however, unclear on the contribution from TM and O due to the hybridization nature between them. The quantification on the p -band intensity, on the other hand, provides an opportunity to directly probe oxygen redox activities. As shown in Figure 8d, the initial p -band intensity is fairly low in the pristine $\text{Li}_{1.3}\text{Nb}_{0.3}\text{Mn}_{0.4}\text{O}_2$ and remains nearly constant below Li content of ~ 0.9 , suggesting negligible interactions between oxygen anions or oxygen redox activities. As x decreases to below 0.9, there is an increase in the p -band intensity, and the trend continues to full delithiation ($x = 0$). The results suggest a continuous increase in oxygen valence states in this region and the participation of oxygen redox for charge compensation. Combined with the results from the Mn K edge XAS spectra which shows that Mn is active when $x > 0.9$ and inactive when $x < 0.9$, the quantification of O K -edge XAS spectra enables the understanding of complete charge compensation mechanism during delithiation of $\text{Li}_{1.3}\text{Nb}_{0.3}\text{Mn}_{0.4}\text{O}_2$ crystals. Note that the p -band intensity in the $x < 0.9$ region is generally higher in the FY mode than that in the TEY mode, consistent with a difference in oxygen activities, likely enhanced lattice O loss on the surface.

The evolution of particle morphology during the first delithiation is revealed by the SEM images collected on the series of delithiated crystal samples (Figure 9). Some surface roughing was observed but the particles remain intact when $x > 0.9$. With further lithium extraction, large cracks begin to appear, which tend to propagate across the entire particle, leading to the eventual fracturing of the crystals. The number of cracks on each crystal increases along with the decrease in x but appears to reach the maximum at a Li content of 0.5–0.6. This coincides with the occurrence of maximum fraction of phase 3, as shown in Figure 6b. The change in morphology is also consistent with the fact that Mn is redox active when $x > 0.9$ while O is redox active when $x < 0.9$. The participation of oxygen redox appears to cause significant morphological damage. Our results also suggest that lattice oxidation of O^{2-} to O^{n-} ($0 < n < 2$) is more damaging than O_2 gas evolution, although it is possible that particles become more stable when x is less than 0.5–0.6 as mechanical stress is released by certain cracks and fractures at that point. Further evaluation on oxygen oxidation and mechanical damage in Li-excess oxides is warranted, but we emphasize that particle cracking and fracturing create fresh surfaces which can contribute to increased O loss from the lattice and side reactions with the electrolyte. Successful surface stabilization strategies such as elemental segregation and coating treatment therefore need to take consideration in particle morphology evolution during cycling.

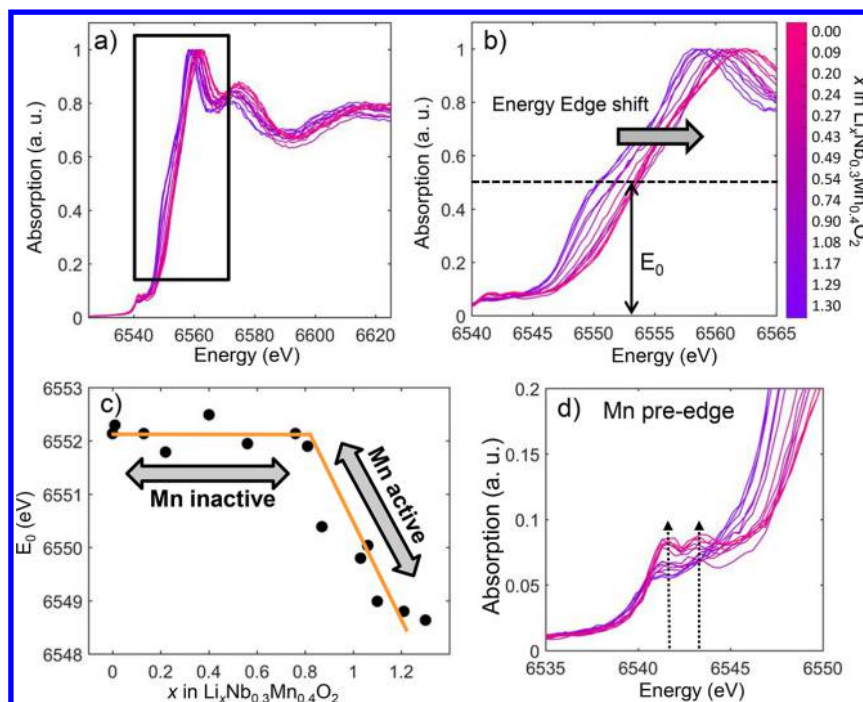


Figure 7. (a and b) Mn *K*-edge hard XAS and XANES spectra, (c) XANES energy edge (E_0) as a function of Li content in $\text{Li}_x\text{Nb}_{0.3}\text{Mn}_{0.4}\text{O}_2$ samples, and (d) Mn *K*-edge pre-edge spectra.

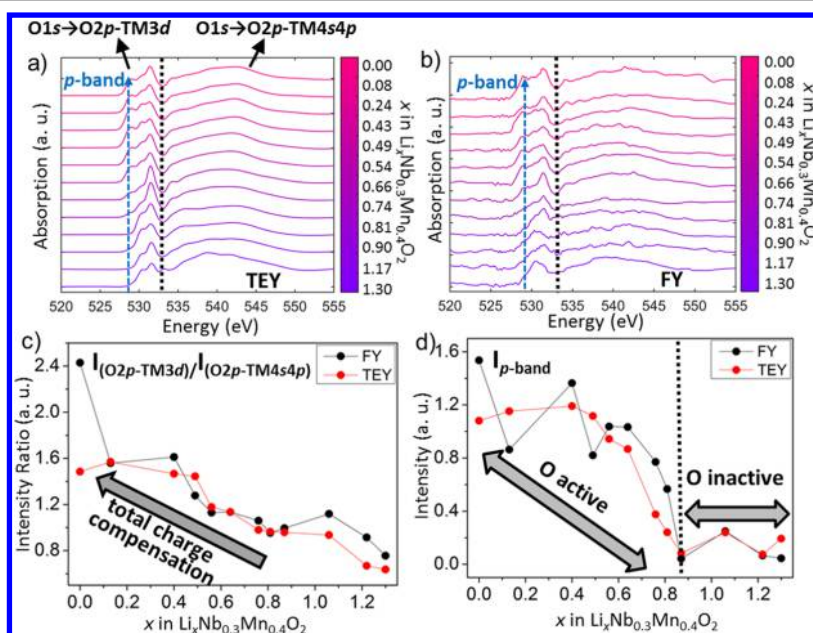


Figure 8. (a and b) O *K*-edge soft XAS spectra obtained in TEY and FY modes, (c) intensity ratio between the pre-edge and postedge absorption peaks as a function of lithium content, and (d) intensity of the *p*-band as a function of lithium content. In panels a and b, black dashed line divides the pre- and postedge regions, and the blue dashed arrow follows the evolution of the *p*-band intensity.

4. CONCLUSION

Disordered, Li-excess transition-metal oxide cathodes are capable of delivering high capacities and are promising next-generation LIB cathodes. In this study, uniform and phase-pure $\text{Li}_{1.3}\text{Nb}_{0.3}\text{Mn}_{0.4}\text{O}_2$ single crystals were synthesized by a molten-salt method for the first time and used as a diagnostic tool to understand the charge compensation mechanism during Li extraction and insertion. Electrochemical evaluation suggests structural irreversibility after the first cycle, leading to capacity and voltage fade of the cathode. Both CO_2 and O_2 gas

evolution was found during the first cycle, with the latter only accounting for $\sim 1\%$ of the charge capacity, in addition to the contribution of $\sim 35\%$ capacity from the $\text{Mn}^{3+/4+}$ redox couple. A large fraction of capacity therefore originates from the redox process of $\text{O}^{2-}/\text{O}^{n-}$ ($0 < n < 2$). Joint refinement on synchrotron X-ray and neutron diffraction patterns of $\text{Li}_x\text{Nb}_{0.3}\text{Mn}_{0.4}\text{O}_2$ series showed that the oxide undergoes a single-phase reaction involving $\text{Mn}^{3+/4+}$ redox reaction when $0.9 < x < 1.3$ and a two-phase reaction involving mixed $\text{O}^{2-}/\text{O}^{n-}$ ($0 \leq n < 2$) reactions when $0 < x < 0.9$. For the fully

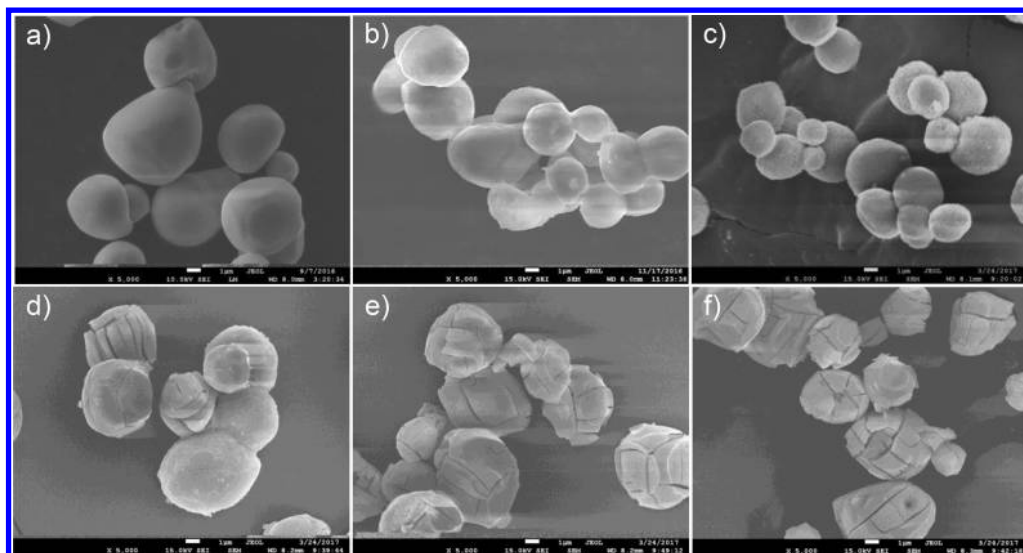


Figure 9. SEM images of chemically delithiated $\text{Li}_x\text{Nb}_{0.3}\text{Mn}_{0.4}\text{O}_2$ crystals: $x =$ (a) 1.3, (b) 1.1, (c) 0.87, (d) 0.76, (e) 0.56, and (f) 0.13.

delithiated sample, ~ 7.8 mol % of oxide-ion vacancies were found, resulting from O loss from the lattice. Cracks and fractures initiated and intensified with deep lithium extraction, which serves as a means to release the mechanical stress endured by the large crystals during the oxygen redox processes.

■ ASSOCIATED CONTENT

Supporting Information

The Supporting Information is available free of charge on the ACS Publications website at DOI: [10.1021/acs.chemmater.7b05036](https://doi.org/10.1021/acs.chemmater.7b05036).

SEM image of carbon mixed $\text{LiNb}_{0.3}\text{Mn}_{0.4}\text{O}_2$ crystals after ball milling, Rietveld refinement of synchrotron X-ray diffraction patterns collected on chemically delithiated $\text{Li}_x\text{Nb}_{0.3}\text{Mn}_{0.4}\text{O}_2$ crystals, Rietveld refinement of synchrotron X-ray and neutron diffraction patterns collected on chemically delithiated $\text{Li}_0\text{Nb}_{0.3}\text{Mn}_{0.4}\text{O}_2$ crystals, and process used to quantify O K -edge XAS data (PDF)

■ AUTHOR INFORMATION

Corresponding Author

*E-mail: gchen@lbl.gov.

ORCID

Wang Hay Kan: 0000-0002-1663-2999

Joseph K. Papp: 0000-0002-7982-6096

Bryan D. McCloskey: 0000-0001-6599-2336

Guoying Chen: 0000-0002-3218-2609

Notes

The authors declare no competing financial interest.

■ ACKNOWLEDGMENTS

We thank Dr. Longjun Li at LBNL for helping with the ICP measurements. Fruitful discussions with Drs. Saravanan Kuppam, Wei Tong, Marca Doeff, and Chixia Tian at LBNL, Dr. Stefan Adams at National University of Singapore, Professor Ian D. Williams at the Hong Kong University of Science and Technology (HKUST), and Dr. Dennis Nordlund at the Stanford Synchrotron Radiation Lightsource (SSRL) are

greatly appreciated. We thank Prof. Naoaki Yabuuchi in Denki University for the helpful suggestions on oxide synthesis. Work at the Molecular Foundry was supported by the Office of Science, Office of Basic Energy Sciences, of the U.S. Department of Energy under Contract DE-AC02-05CH11231. The POWGEN beamline at ORNL is sponsored by the Scientific User Facilities Division, Office of Basic Energy Sciences, U.S. Department of Energy. Use of the Stanford Synchrotron Radiation Lightsource, SLAC National Accelerator Laboratory, is supported by the U.S. Department of Energy, Office of Science, Office of Basic Energy Sciences under Contract DE-AC02-76SF00515. This work was supported by the Assistant Secretary for Energy Efficiency and Renewable Energy, Office of FreedomCAR and Vehicle Technologies of the U.S. Department of Energy under Contract DE-AC02-05CH11231.

■ REFERENCES

- (1) Goodenough, J. B.; Manthiram, A. A perspective on electrical energy storage. *MRS Commun.* **2014**, *4*, 135–142.
- (2) Li, W.; Song, B.; Manthiram, A. High-voltage positive electrode materials for lithium-ion batteries. *Chem. Soc. Rev.* **2017**, *46*, 3006–3059.
- (3) Manthiram, A.; Knight, J. C.; Myung, S.-T.; Oh, S.-M.; Sun, Y.-K. Nickel-Rich and Lithium-Rich Layered Oxide Cathodes: Progress and Perspectives. *Adv. Energy Mater.* **2016**, *6*, 1501010.
- (4) Aydinol, M. K.; Kohan, A. F.; Ceder, G.; Cho, K.; Joannopoulos, J. Ab initio study of lithium intercalation in metal oxides and metal dichalcogenides. *Phys. Rev. B: Condens. Matter Mater. Phys.* **1997**, *56*, 1354–1365.
- (5) McCalla, E.; Abakumov, A. M.; Saubanere, M.; Foix, D.; Berg, E. J.; Rousse, G.; Doublet, M.-L.; Gonbeau, D.; Novak, P.; Van Tendeloo, G.; Dominko, R.; Tarascon, J.-M. Visualization of O-O peroxo-like dimers in high-capacity layered oxides for Li-ion batteries. *Science (Washington, DC, U. S.)* **2015**, *350*, 1516–1521.
- (6) Pearce, P. E.; Perez, A. J.; Rousse, G.; Saubanere, M.; Batuk, D.; Foix, D.; McCalla, E.; Abakumov, A. M.; Van Tendeloo, G.; Doublet, M.-L.; Tarascon, J.-M. Evidence for anionic redox activity in a tridimensional-ordered Li-rich positive electrode $\beta\text{-Li}_2\text{IrO}_3$. *Nat. Mater.* **2017**, *16*, 580–586.
- (7) Sathiyaa, M.; Rousse, G.; Ramesha, K.; Laisa, C. P.; Vezin, H.; Sougrati, M. T.; Doublet, M. L.; Foix, D.; Gonbeau, D.; Walker, W.; Prakash, A. S.; Ben Hassine, M.; Dupont, L.; Tarascon, J. M. Reversible

anionic redox chemistry in high-capacity layered-oxide electrodes. *Nat. Mater.* **2013**, *12*, 827–835.

(8) Armstrong, A. R.; Holzapfel, M.; Novak, P.; Johnson, C. S.; Kang, S.-H.; Thackeray, M. M.; Bruce, P. G. Demonstrating Oxygen Loss and Associated Structural Reorganization in the Lithium Battery Cathode $\text{Li}[\text{Ni}_{0.2}\text{Li}_{0.2}\text{Mn}_{0.6}]\text{O}_2$. *J. Am. Chem. Soc.* **2006**, *128*, 8694–8698.

(9) Luo, K.; Roberts, M. R.; Guerrini, N.; Tapia-Ruiz, N.; Hao, R.; Massel, F.; Pickup, D. M.; Ramos, S.; Liu, Y.-S.; Guo, J.; Chadwick, A. V.; Duda, L. C.; Bruce, P. G. Anion Redox Chemistry in the Cobalt Free 3d Transition Metal Oxide Intercalation Electrode $\text{Li}[\text{Li}_{0.2}\text{Ni}_{0.2}\text{Mn}_{0.6}]\text{O}_2$. *J. Am. Chem. Soc.* **2016**, *138*, 11211–11218.

(10) Luo, K.; Roberts, M. R.; Hao, R.; Guerrini, N.; Pickup, D. M.; Liu, Y.-S.; Edstrom, K.; Guo, J.; Chadwick, A. V.; Duda, L. C.; Bruce, P. G. Charge-compensation in 3d-transition-metal-oxide intercalation cathodes through the generation of localized electron holes on oxygen. *Nat. Chem.* **2016**, *8*, 684–691.

(11) Shukla, A. K.; Ramasse, Q. M.; Ophus, C.; Duncan, H.; Hage, F.; Chen, G. Unravelling structural ambiguities in lithium- and manganese-rich transition metal oxides. *Nat. Commun.* **2015**, *6*, 8711.

(12) Mohanty, D.; Li, J.; Abraham, D. P.; Huq, A.; Payzant, E. A.; Wood, D. L.; Daniel, C. Unraveling the Voltage-Fade Mechanism in High-Energy-Density Lithium-Ion Batteries: Origin of the Tetrahedral Cations for Spinel Conversion. *Chem. Mater.* **2014**, *26*, 6272–6280.

(13) Wang, D.; Huang, Y.; Huo, Z.; Chen, L. Synthesize and electrochemical characterization of Mg-doped Li-rich layered $\text{Li}[\text{Li}_{0.2}\text{Ni}_{0.2}\text{Mn}_{0.6}]\text{O}_2$ cathode material. *Electrochim. Acta* **2013**, *107*, 461–466.

(14) Song, B.; Zhou, C.; Wang, H.; Liu, H.; Liu, Z.; Lai, M. O.; Lu, L. Advances in sustain stable voltage of Cr-doped Li-rich layered cathodes for lithium ion batteries. *J. Electrochem. Soc.* **2014**, *161*, A1723–A1730.

(15) Li, G. R.; Feng, X.; Ding, Y.; Ye, S. H.; Gao, X. P. AlF₃-coated $\text{Li}(\text{Li}_{0.17}\text{Ni}_{0.25}\text{Mn}_{0.58})\text{O}_2$ as cathode material for Li-ion batteries. *Electrochim. Acta* **2012**, *78*, 308–315.

(16) Shi, S. J.; Tu, J. P.; Tang, Y. Y.; Liu, X. Y.; Zhang, Y. Q.; Wang, X. L.; Gu, C. D. Enhanced cycling stability of $\text{Li}[\text{Li}_{0.2}\text{Mn}_{0.54}\text{Ni}_{0.13}\text{Co}_{0.13}]\text{O}_2$ by surface modification of MgO with melting impregnation method. *Electrochim. Acta* **2013**, *88*, 671–679.

(17) Zhang, X.; Belharouak, I.; Li, L.; Lei, Y.; Elam, J. W.; Nie, A.; Chen, X.; Yassar, R. S.; Axelbaum, R. L. Structural and Electrochemical Study of Al_2O_3 and TiO_2 Coated $\text{Li}_{1.2}\text{Ni}_{0.13}\text{Mn}_{0.54}\text{Co}_{0.13}\text{O}_2$ Cathode Material Using ALD. *Adv. Energy Mater.* **2013**, *3*, 1299–1307.

(18) Kim, K. J.; Jo, Y. N.; Lee, W. J.; Subburaj, T.; Prasanna, K.; Lee, C. W. Effects of inorganic salts on the morphological, structural, and electrochemical properties of prepared nickel-rich $\text{Li}[\text{Ni}_{0.6}\text{Co}_{0.2}\text{Mn}_{0.2}]\text{O}_2$. *J. Power Sources* **2014**, *268*, 349–355.

(19) Shigemura, H.; Tabuchi, M.; Sakaebe, H.; Kobayashi, H.; Kageyama, H. Lithium Extraction and Insertion Behavior of Nanocrystalline Li_2TiO_3 - LiFeO_2 Solid Solution with Cubic Rock Salt Structure. *J. Electrochem. Soc.* **2003**, *150*, A638–A644.

(20) Tabuchi, M.; Nakashima, A.; Shigemura, H.; Ado, K.; Kobayashi, H.; Sakaebe, H.; Tatsumi, K.; Kageyama, H.; Nakamura, T.; Kanno, R. Fine $\text{Li}_{(4-x)/3}\text{Ti}_{(2-2x)/3}\text{Fe}_x\text{O}_2$ ($0.18 \leq x \leq 0.67$) powder with cubic rock-salt structure as a positive electrode material for rechargeable lithium batteries. *J. Mater. Chem.* **2003**, *13*, 1747–1757.

(21) Lee, J.; Urban, A.; Li, X.; Su, D.; Hautier, G.; Ceder, G. Unlocking the Potential of Cation-Disordered Oxides for Rechargeable Lithium Batteries. *Science (Washington, DC, U. S.)* **2014**, *343*, 519–522.

(22) Yabuuchi, N.; Takeuchi, M.; Nakayama, M.; Shiiba, H.; Ogawa, M.; Nakayama, K.; Ohta, T.; Endo, D.; Ozaki, T.; Inamasu, T.; Sato, K.; Komaba, S. High-capacity electrode materials for rechargeable lithium batteries: Li_3NbO_4 -based system with cation-disordered rocksalt structure. *Proc. Natl. Acad. Sci. U. S. A.* **2015**, *112*, 7650–7655.

(23) Toby, B. H. EXPGUI, a graphical user interface for GSAS. *J. Appl. Crystallogr.* **2001**, *34*, 210–213.

(24) Xu, J.; Renfrew, S.; Marcus, M. A.; Sun, M.; McCloskey, B. D.; Tong, W. Investigating Li_2NiO_2 - Li_2CuO_2 Solid Solutions as High-

Capacity Cathode Materials for Li-Ion Batteries. *J. Phys. Chem. C* **2017**, *121*, 11100–11107.

(25) Edington, J. W. *Practical Electron Microscopy in Materials Science*; Van Nostrand Reinhold Co., 1976.

(26) Renfrew, S.; McCloskey, B. D. Residual lithium carbonate predominantly accounts for first cycle CO_2 and CO outgassing of Li-stoichiometric and Li-rich layered transition metal oxides. *J. Am. Chem. Soc.* **2017**, *139*, 17853–17860.

(27) Freunberger, S. A.; Chen, Y.; Peng, Z.; Griffin, J. M.; Hardwick, L. J.; Barde, F.; Novak, P.; Bruce, P. G. Reactions in the Rechargeable Lithium- O_2 Battery with Alkyl Carbonate Electrolytes. *J. Am. Chem. Soc.* **2011**, *133*, 8040–8047.

(28) Aurbach, D.; Daroux, M.; Faguy, P.; Yeager, E. The electrochemistry of noble metal electrodes in aprotic organic solvents containing lithium salts. *J. Electroanal. Chem. Interfacial Electrochem.* **1991**, *297*, 225–44.

(29) Aurbach, D.; Gofer, Y.; Langzam, J. The correlation between surface chemistry, surface morphology, and cycling efficiency of lithium electrodes in a few polar aprotic systems. *J. Electrochem. Soc.* **1989**, *136*, 3198.

(30) Choi, J.; Alvarez, E.; Arunkumar, T. A.; Manthiram, A. Proton insertion into oxide cathodes during chemical delithiation. *Electrochem. Solid-State Lett.* **2006**, *9*, A241–A244.

(31) Terada, Y.; Yasaka, K.; Nishikawa, F.; Konishi, T.; Yoshio, M.; Nakai, I. In Situ XAFS Analysis of $\text{Li}(\text{Mn},\text{M})_2\text{O}_4$ ($\text{M} = \text{Cr}, \text{Co}, \text{Ni}$) 5 V Cathode Materials for Lithium-Ion Secondary Batteries. *J. Solid State Chem.* **2001**, *156*, 286–291.

(32) Nam, K.-W.; Bak, S.-M.; Hu, E.; Yu, X.; Zhou, Y.; Wang, X.; Wu, L.; Zhu, Y.; Chung, K.-Y.; Yang, X.-Q. Combining In Situ Synchrotron X-Ray Diffraction and Absorption Techniques with Transmission Electron Microscopy to Study the Origin of Thermal Instability in Overcharged Cathode Materials for Lithium-Ion Batteries. *Adv. Funct. Mater.* **2013**, *23*, 1047–1063.

(33) Hu, E.; Bak, S.-M.; Liu, J.; Yu, X.; Zhou, Y.; Ehrlich, S. N.; Yang, X.-Q.; Nam, K.-W. Oxygen-Release-Related Thermal Stability and Decomposition Pathways of $\text{Li}_x\text{Ni}_{0.5}\text{Mn}_{1.5}\text{O}_4$ Cathode Materials. *Chem. Mater.* **2014**, *26*, 1108–1118.

(34) Kim, M. G.; Shin, H. J.; Kim, J.-H.; Park, S.-H.; Sun, Y.-K. XAS Investigation of Inhomogeneous Metal-Oxygen Bond Covalency in Bulk and Surface for Charge Compensation in Li-Ion Battery Cathode $\text{Li}[\text{Ni}_{1/3}\text{Co}_{1/3}\text{Mn}_{1/3}]\text{O}_2$ Material. *J. Electrochem. Soc.* **2005**, *152*, A1320–A1328.

(35) Kim, M. G.; Yo, C. H. X-ray Absorption Spectroscopic Study of Chemically and Electrochemically Li Ion Extracted $\text{Li}_y\text{Co}_{0.85}\text{Al}_{0.15}\text{O}_2$ Compounds. *J. Phys. Chem. B* **1999**, *103*, 6457–6465.

(36) Ignatov, A. Y.; Ali, N.; Khalid, S. Mn K-edge XANES study of the $\text{La}_{1-x}\text{Ca}_x\text{MnO}_3$ colossal magnetoresistive manganites. *Phys. Rev. B: Condens. Matter Mater. Phys.* **2001**, *64*, 014413/1–014413/16.

(37) Stöhr, J. *NEXAFS Spectroscopy*; Springer, 1992.

(38) Yoon, W.-S.; Balasubramanian, M.; Chung, K. Y.; Yang, X.-Q.; McBreen, J.; Grey, C. P.; Fischer, D. A. Investigation of the Charge Compensation Mechanism on the Electrochemically Li-Ion Deintercalated $\text{Li}_{1-x}\text{Co}_{1/3}\text{Ni}_{1/3}\text{Mn}_{1/3}\text{O}_2$ Electrode System by Combination of Soft and Hard X-ray Absorption Spectroscopy. *J. Am. Chem. Soc.* **2005**, *127*, 17479–17487.

(39) de Groot, F. M. F.; Grioni, M.; Fuggle, J. C.; Ghijsen, J.; Sawatzky, G. A.; Petersen, H. Oxygen 1s x-ray-absorption edges of transition-metal oxides. *Phys. Rev. B: Condens. Matter Mater. Phys.* **1989**, *40*, 5715–5723.

(40) Oishi, M.; Yamanaka, K.; Watanabe, I.; Shimoda, K.; Matsunaga, T.; Arai, H.; Ukyo, Y.; Uchimoto, Y.; Ogumi, Z.; Ohta, T. Direct observation of reversible oxygen anion redox reaction in Li-rich manganese oxide, Li_2MnO_3 , studied by soft X-ray absorption spectroscopy. *J. Mater. Chem. A* **2016**, *4*, 9293–9302.

(41) Ma, C.; Alvarado, J.; Xu, J.; Clément, R. J.; Kodur, M.; Tong, W.; Grey, C. P.; Meng, Y. S. Exploring Oxygen Activity in the High Energy P2-Type $\text{Na}_{0.78}\text{Ni}_{0.23}\text{Mn}_{0.69}\text{O}_2$ Cathode Material for Na-Ion Batteries. *J. Am. Chem. Soc.* **2017**, *139*, 4835–4845.

(42) Kang, J. S.; Kim, D. H.; Hwang, J. H.; Baik, J.; Shin, H. J.; Kim, M.; Jeong, Y. H.; Min, B. I. Soft x-ray absorption and photoemission spectroscopy study of superoxide KO_2 . *Phys. Rev. B: Condens. Matter Mater. Phys.* **2010**, *82*, 193102.

(43) Yilmaz, E.; Yogi, C.; Yamanaka, K.; Ohta, T.; Byon, H. R. Promoting Formation of Noncrystalline Li_2O_2 in the $\text{Li}-\text{O}_2$ Battery with RuO_2 Nanoparticles. *Nano Lett.* **2013**, *13*, 4679–4684.